



Launching graphene surface plasmon waves with vanishingly small periodic grating structures

DAVID P. NICHOLLS^{1,*}  AND SANG-HYUN OH²

¹Department of Mathematics, Statistics, and Computer Science, University of Illinois at Chicago, Chicago, Illinois 60607, USA

²Department of Electrical and Computer Engineering, University of Minnesota, Minneapolis, Minnesota 55455, USA

*Corresponding author: davidn@uic.edu

Received 10 August 2020; revised 16 February 2021; accepted 2 March 2021; posted 3 March 2021 (Doc. ID 404896); published 25 March 2021

Graphene is now a crucial component of many device designs in electronics and optics. Just like the noble metals, this single layer of carbon atoms in a honeycomb lattice can support surface plasmons, which are central to several sensing technologies in the mid-infrared regime. As with classical metal plasmons, periodic corrugations in the graphene sheet itself can be used to launch these surface waves; however, as graphene plasmons are tightly confined, the role of unwanted surface roughness, even at a nanometer scale, cannot be ignored. In this work, we revisit our previous numerical experiments on metal plasmons launched by vanishingly small grating structures, with the addition of graphene to the structure. These simulations are conducted with a recently devised, rapid, and robust high-order spectral scheme of the authors, and with it we carefully demonstrate how the plasmonic response of a perfectly flat sheet of graphene can be significantly altered with even a tiny corrugation (on the order of merely 5 nm). With these results, we demonstrate the primary importance of fabrication techniques that produce interfaces whose deviations from flat are on the order of angstroms. © 2021 Optical Society of America

<https://doi.org/10.1364/JOSAA.404896>

1. INTRODUCTION

Graphene, a single-atom-thick sheet of carbon, has benefited many applications in electronics and optics [1]. Analogous to noble metals, graphene can also sustain charge density fluctuations called plasmons [2], which can dramatically enhance light-matter interactions. Graphene plasmons typically reside in the mid-infrared spectral range (2–30 μm in wavelength) and can exhibit much shorter wavelengths (hence higher momenta) compared with free-space light at a given frequency. Due to their tightly confined evanescent fields, graphene plasmons are very effective for sensing, spectroscopy, and photodetection. We direct the interested reader to recent work on graphene and other two-dimensional materials [3–6] and surveys [7–12] for more details about the theory and uses of graphene in optical devices.

After initial observations of graphene plasmons in the mid-infrared via scattering near-field optical microscopy [13,14], researchers have explored practical schemes to launch and detect graphene plasmons via far-field techniques. As with the excitation of conventional metal plasmons, periodic modulation of graphene itself or the surrounding dielectric environment can be employed. Since graphene plasmons are tightly confined, the role of unwanted surface roughness, even at a nanometer scale, cannot be ignored. In this work, we revisit our previous numerical experiments on noble metal plasmons launched by vanishingly small grating structures [15] with the addition of

graphene to the structure. For this, we use the recently devised code of Nicholls [16] and quantify how nanometric gratings influence the efficiency of launching graphene plasmons.

Our numerical scheme is, by no means, the only alternative for this investigation. For instance, the finite element simulations in [17] investigated the excitation of graphene plasmons by a point source, while [18] describes a finite element method coupled to an adaptive mesh refinement strategy to capture the field in a small neighborhood of the graphene sheet. We also note finite element simulations of edge effects [19] and the epsilon near zero (ENZ) effect [20]. Please see the survey paper [21] for a complete discussion of approaches that have been utilized in the engineering literature.

As we demonstrate with careful numerical experiments, the plasmonic response of a perfectly flat sheet of graphene can be significantly altered with even a tiny deterministic sinusoidal corrugation on the order of merely 5 nm. In fact, there can be quite a noticeable effect when even a minuscule 1 nm deformation is affected. With these observations, we demonstrate quite conclusively the supreme importance of using sophisticated fabrication techniques that produce interfaces whose deviations from flat, be they deterministic or random, are on the order of angstroms.

The rest of the paper is organized as follows. The governing equations are briefly reviewed in Section 2 together with our model for the graphene in Section 2.A, and the surface

formulation that we utilize in Section 2.B. Our numerical method is briefly described in Section 3, while we present the results of our numerical simulations in Section 4. Concluding remarks are given in Section 5. Finally, we discuss the dispersion relation of graphene plasmons in terms of our formulation in Appendix A.

2. GOVERNING EQUATIONS

We consider the simplest configuration to study the limits of corrugation size in the excitation of graphene surface plasmon resonances (GSPRs): a y -invariant, laterally periodic, doubly-layered medium with an infinitesimally thin layer of graphene at the interface. This interface is periodic and shaped by

$$z = g(x), \quad g(x+d) = g(x)$$

(Fig. 1), with permittivity (refractive index) $\epsilon^{(u)}$ ($n^{(u)}$) in $\{z > g(x)\}$ and $\epsilon^{(w)}$ ($n^{(w)}$) in $\{z < g(x)\}$.

We further specify that the structure be illuminated from above by transversely aligned monochromatic plane-wave radiation of frequency ω and wavenumber $k^{(u)} = n^{(u)}\omega/c_0 = \omega/c^{(u)}$ (c_0 is the speed of light), e.g., in transverse magnetic (TM) polarization:

$$\mathbf{H}^{\text{inc}} = (0 \ 1 \ 0)^T \exp(i\alpha x - i\gamma^{(u)} z),$$

$$\alpha = k^{(u)} \sin(\theta), \quad \gamma^{(u)} = k^{(u)} \cos(\theta).$$

The reduced electric and magnetic fields satisfy the time-harmonic Maxwell equations, and the incident radiation generates reflected and transmitted fields above and below the interface. It is well known [22,23] that the full fields can be recovered from the transverse (y) component of the field, e.g., in TM polarization:

$$v(x, z) = \begin{cases} u(x, z), & z > g(x), \\ w(x, z), & z < g(x), \end{cases}$$

which is quasiperiodic:

$$u(x+d, z) = e^{i\alpha d} u(x, z), \quad w(x+d, z) = e^{i\alpha d} w(x, z).$$

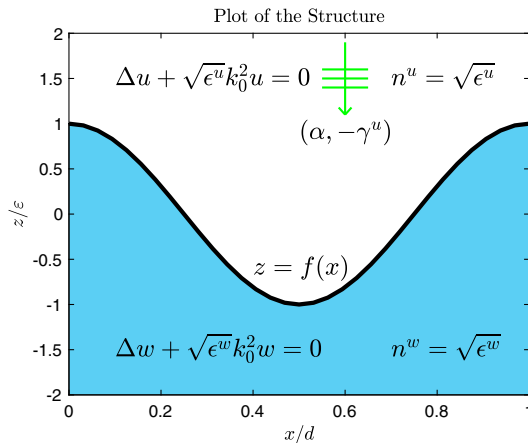


Fig. 1. Depiction of the structures under consideration: graphene mounted on vacuum, ion gel, or silica under vacuum. Structure rescaled by the period in the x coordinate and the maximum amplitude in the z coordinate.

Across the interface, the tangential component of the electric field is continuous, while the presence of the graphene sheet gives a jump in the tangential component of the magnetic field equal to the surface current (see [16] and references therein). As in [16], we model this current as proportional to the *tangential* component of the surface electric field with proportionality constant $\sigma^{(g)}$.

As we have shown in [16], these considerations lead us to solve, in TM polarization, the system of equations

$$\Delta u + \epsilon^{(u)} k_0^2 u = 0, \quad z > g(x), \quad (1a)$$

$$\Delta w + \epsilon^{(w)} k_0^2 w = 0, \quad z < g(x), \quad (1b)$$

$$|\mathbf{N}|u - \left\{ |\mathbf{N}| - \frac{\hat{\sigma}^{(g)}}{ik_0\epsilon^{(w)}} \partial_N \right\} w = |\mathbf{N}|\xi, \quad z = g(x), \quad (1c)$$

$$\frac{1}{\epsilon^{(u)}} \partial_N u - \frac{1}{\epsilon^{(w)}} \partial_N w = \frac{1}{\epsilon^{(u)}} \nu, \quad z = g(x), \quad (1d)$$

where we have reduced the time-harmonic Maxwell equations to Helmholtz equations for the transverse components of the magnetic field, and $\hat{\sigma}^{(g)} = \sigma^{(g)}/(\epsilon_0 c_0)$ is the non-dimensional current. In these,

$$\xi = -(u^{\text{inc}})_{z=g}, \quad \nu = -(\partial_N u^{\text{inc}})_{z=g},$$

$$\mathbf{N} = (-\partial_x g \ 0 \ 1)^T, \quad \partial_N = \mathbf{N} \cdot \nabla. \quad (1e)$$

A. Graphene Model

For the layer of graphene, we use the Drude model for the current presented in [24]:

$$\hat{\sigma}^{(g)} = \frac{\sigma^{(g)}}{\epsilon_0 c_0}, \quad \sigma^{(g)} = \sigma_0 \left(\frac{4E_F/\pi}{\Gamma - i\hbar\omega} \right), \quad \sigma_0 := \pi\epsilon_0 c_0 \alpha;$$

here α is the fine-structure constant, E_F is the (local) Fermi level position, and $\Gamma := \hbar\gamma$, where \hbar is the reduced Planck's constant, and γ is the relaxation rate. In our simulations, we used

$$E_F = 0.45 \text{ eV}, \quad \Gamma = 2.6 \times 10^{-3} \text{ eV}.$$

B. Surface Formulation

To further specify our approach to simulating solutions of this two-layer, graphene structure, we state our surface formulation first presented in [16]. To begin, we define the Dirichlet traces

$$U(x) := u(x, g(x)), \quad W(x) := w(x, g(x)),$$

the (exterior pointing) Neumann traces

$$\tilde{U}(x) := -(\partial_N u)(x, g(x)), \quad \tilde{W}(x) := (\partial_N w)(x, g(x)),$$

and the Dirichlet–Neumann operators (DNOs)

$$G(g) : U(x) \rightarrow \tilde{U}(x), \quad J(g) : W(x) \rightarrow \tilde{W}(x),$$

which encode the fact that u and w solve their respective Helmholtz problems, Eqs. (1a) and (1b). In terms of these, we write Eq. (1) as

$$|\mathbf{N}|U - \left\{ |\mathbf{N}| - \frac{\hat{\sigma}^{(g)}}{ik_0\epsilon^{(w)}}J \right\} W = |\mathbf{N}|\xi, \\ -\frac{1}{\epsilon^{(u)}}G[U] - \frac{1}{\epsilon^{(w)}}J[W] = \frac{1}{\epsilon^{(u)}}\nu,$$

or, equivalently (after negating the second equation),

$$\mathbf{A}\mathbf{V} = \mathbf{R}, \quad (2a)$$

where [25]

$$\mathbf{A} := \begin{pmatrix} |\mathbf{N}| & -|\mathbf{N}| + \frac{\hat{\sigma}^{(g)}}{ik_0\epsilon^{(w)}}J \\ \frac{1}{\epsilon^{(u)}}G & \frac{1}{\epsilon^{(w)}}J \end{pmatrix}, \\ \mathbf{V} = \begin{pmatrix} U \\ W \end{pmatrix}, \quad \mathbf{R} = \begin{pmatrix} |\mathbf{N}|\xi \\ -\frac{1}{\epsilon^{(u)}}\nu \end{pmatrix}. \quad (2b)$$

We use this surface formulation for a number of reasons. Primarily, it is due to the fact that it reduces the *volumetric* statement of the problem, Eq. (1), to a *surface* formulation, Eq. (2), which enables an *enormous* saving of memory and execution time in the numerical scheme that we briefly outline below. In addition, it gives us access to the theoretical tools developed in [25], which may be of interest.

Before outlining our numerical scheme, we recall the classical dispersion relation for graphene surface plasmons:

$$\frac{\epsilon^{(u)}}{\kappa^{(u)}} + \frac{\epsilon^{(w)}}{\kappa^{(w)}} + \frac{i\hat{\sigma}^{(g)}}{k_0} = 0,$$

cf. Eq. (6). For a full derivation in our modern formulation, please see Appendix A, which also describes the base case upon which our scheme is built.

3. NUMERICAL METHOD

We now briefly describe the numerical procedure outlined in our previous work [16]. Our governing equations, Eq. (2), for the surface unknowns $\{U, W\}$ are $\mathbf{A}\mathbf{V} = \mathbf{R}$. At this point, we take a *perturbative* point of view by assuming that the interfacial boundary, $g(x)$, is a *small* deviation from the (trivial) flat configuration, which we make precise as

$$g(x) = \varepsilon f(x), \quad \varepsilon \ll 1.$$

It is of great importance that the restriction of ε *small* can be lifted provided that ε is *real* [26]. With this assumption, it can be shown that not only do the operator \mathbf{A} and function \mathbf{R} depend *analytically* upon ε , so that

$$\{\mathbf{A}, \mathbf{R}\} = \{\mathbf{A}, \mathbf{R}\}(\varepsilon) = \sum_{n=0}^{\infty} \{\mathbf{A}_n, \mathbf{R}_n\} \varepsilon^n,$$

but also that a unique solution of the form

$$\mathbf{V} = \mathbf{V}(\varepsilon) = \sum_{n=0}^{\infty} \mathbf{V}_n \varepsilon^n$$

satisfies Eq. (2) [25]. Furthermore, the solution is given by

$$\mathbf{V}_0 = \mathbf{A}_0^{-1} \mathbf{R}_0 \quad (3)$$

at order $n = 0$, and

$$\mathbf{V}_n = \mathbf{A}_0^{-1} \left\{ \mathbf{R}_n - \sum_{\ell=0}^{n-1} \mathbf{A}_{n-\ell} \mathbf{V}_\ell \right\} \quad (4)$$

for $n > 0$. Importantly, the order-zero operator

$$\mathbf{A}_0 := \begin{pmatrix} I & -I + \frac{\hat{\sigma}^{(g)}}{ik_0\epsilon^{(w)}}J(0) \\ \frac{1}{\epsilon^{(u)}}G(0) & \frac{1}{\epsilon^{(w)}}J(0) \end{pmatrix}$$

corresponds to the flat-interface configuration that can be solved with a classical formula [23] quite rapidly by the fast Fourier transform (FFT) algorithm [27].

Our scheme is a high-order spectral (HOS) approach [27,28] that approximates

$$\{U(x, z), W(x, z)\} \approx \{U^{N_x, N}(x, z), W^{N_x, N}(x, z)\}$$

$$:= \sum_{n=0}^N \sum_{p=-N_x/2}^{N_x/2-1} \{\hat{U}_{n,p}, \hat{W}_{n,p}\} e^{i\alpha_p x} \varepsilon^n. \quad (5)$$

The unknowns $\{\hat{U}_{n,p}, \hat{W}_{n,p}\}$ are determined by enforcing Eqs. (3) and (4) at the collocation points $x_j = 2\pi j/d$ for $j = 0, \dots, N_x - 1$. The nonlinearities on the right-hand sides of Eqs. (3) and (4) are formed by straightforward pointwise multiplication, while the operators \mathbf{A}_0^{-1} can be implemented efficiently by the FFT, as this operator is diagonalized by the Fourier transform. The terms G_ℓ and J_ℓ in the expansion of the DNOs are evaluated by the transformed field expansions (TFEs) method as outlined in [16].

As we noted in [16], a crucial decision must be made in selecting a method to sum the truncated Taylor series (in n) that appears in Eq. (5). In addition, to direct (Taylor) summation, the analytic continuation method of Padé approximation [29] has been very successful when applied to HOPS algorithms [16]. This approximant has notable properties, among which are that, for a wide class of functions, not only is the convergence faster at points of analyticity, but also it may converge for points *outside* the disk of convergence. We refer the reader to Section 2.B of [29] and Section 8.3 of Bender and Orszag [30] for a complete discussion.

4. SIMULATION RESULTS

To study the question of the detectable limits of corrugations in graphene sheets, we investigated three configurations. The geometry of each is the same, but we assemble them out of different materials. In all cases, we illuminated the structure through vacuum above the layer interface that contained the (infinitesimally) thin graphene sheet. Below this, we mounted the structure on one of three dielectrics inspired by vacuum, ion gel, or silica. More specifically, we considered the following three configurations.

1. Vacuum overlaying graphene mounted on vacuum (VGV) with $\epsilon^{(w)} = \epsilon^{(u)} = 1$.
2. Vacuum overlaying graphene mounted on a dielectric with permittivity $\epsilon^{(w)} = 3$, which approximates an ion gel (VGlg) [31].
3. Vacuum overlaying graphene mounted on a dielectric with permittivity $\epsilon^{(w)} = 4$ meant to simulate silica (VGS) [31].

Each of these has the same geometrical parameters:

$$d = 0.530 \text{ } \mu\text{m}, \quad z = \varepsilon f(x) = \varepsilon \cos(2\pi x/d),$$

$$\varepsilon = \varepsilon_{\max} = d/100 = 0.005.$$

We now discuss our results on the dispersion relations, Δ from Eq. (A1), and any enhancements that corrugations in the graphene sheet provided.

To make these enhancements precise, we recall that in a flat-interface configuration, the reflected and transmitted fields will have the forms

$$u(x, z) = Re^{i\alpha x + i\gamma^{(u)}z}, \quad w(x, z) = Te^{i\alpha x - i\gamma^{(w)}z},$$

respectively. From these, we define the (specular) efficiencies

$$B = |R|^2, \quad C = \left(\frac{\gamma^{(w)}}{\gamma^{(u)}} \right) |T|^2.$$

There is a principle of conservation of energy that states that if $\epsilon^{(u)}, \epsilon^{(w)} \in \mathbf{R}^+$ and $\sigma^{(g)} \equiv 0$, then, in TM polarization,

$$B + \left(\frac{\epsilon^{(u)}}{\epsilon^{(w)}} \right) C = 1.$$

So, we define the absorbance

$$A := 1 - B - \left(\frac{\epsilon^{(u)}}{\epsilon^{(w)}} \right) C$$

as the energy lost to the structure (which is zero for two dielectrics in the absence of graphene). When graphene is introduced, then $A > 0$, even in the flat configuration; however, as we will now show, it can be the case that $A(\lambda, \varepsilon) \gg A(\lambda, 0)$ even for quite *small* ε , on the order of just a couple nanometers! To quantify this, we study the ‘‘absorbance map’’:

$$a(\lambda, \varepsilon) := \frac{A(\lambda, \varepsilon)}{A(\lambda, 0)}.$$

A. Vacuum–Graphene–Vacuum Configuration

We began with the vacuum–graphene–vacuum (VGV) configuration and studied first the dispersion relation, Eq. (A1). More specifically, in Figs. 2 and 3, we display $\log \text{Re}\{\Delta\}$ versus (q, ν) and (d, λ) , respectively.

These plots indicate the approximate locations of GSPRs in either (q, ν) or (d, λ) space, which informed our subsequent choices of simulation parameters. With these, we generated the complete plot of the absorbance map for all values $0 \leq \varepsilon \leq \varepsilon_{\max}$ in Fig. 4, and for the final slice at $\varepsilon = \varepsilon_{\max}$ in Fig. 5.

Here we saw a very modest 1.2% enhancement in the absorbance (versus the flat-interface configuration) with

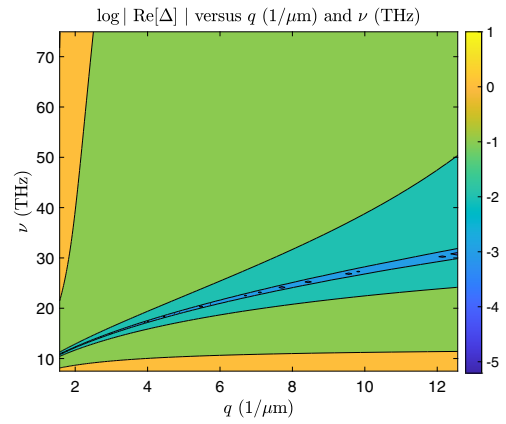


Fig. 2. Plot of the level sets of the natural logarithm of the absolute value of the real part of the dispersion relation, Δ from Eq. (A1), for the VGV configuration, $\epsilon^{(w)} = 1$. Graphene parameter choices are $E_F = 0.45$ eV and $\Gamma = 2.6 \times 10^{-3}$ eV. Contour plots versus q (wavenumber of surface wave) and ν (illumination frequency).

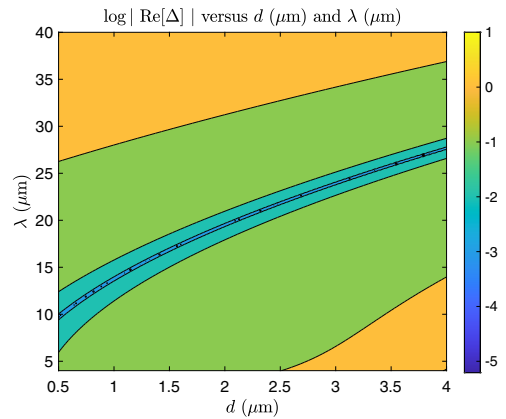


Fig. 3. Plot of the level sets of the natural logarithm of the absolute value of the real part of the dispersion relation, Δ from Eq. (A1), for the VGV configuration, $\epsilon^{(w)} = 1$. Graphene parameter choices are $E_F = 0.45$ eV and $\Gamma = 2.6 \times 10^{-3}$ eV. Contour plots versus d (period of surface wave) and λ (illumination wavelength).

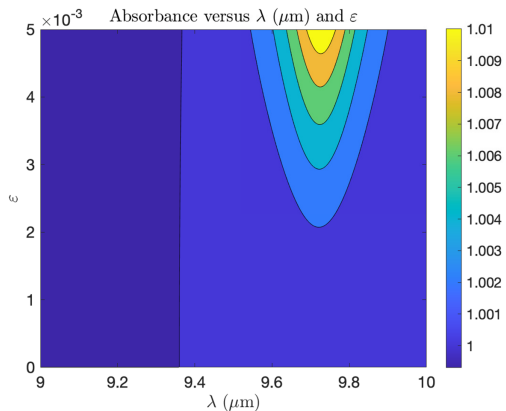


Fig. 4. Complete plot of the absorbance map for the VGV configuration: contour plot of the relative absorbance $a(\lambda, \varepsilon) = A(\lambda, \varepsilon)/A(\lambda, 0)$ versus λ (illumination wavelength) and ε (amplitude of the graphene sheet deformation). Graphene parameter choices are $E_F = 0.45$ eV and $\Gamma = 2.6 \times 10^{-3}$ eV.

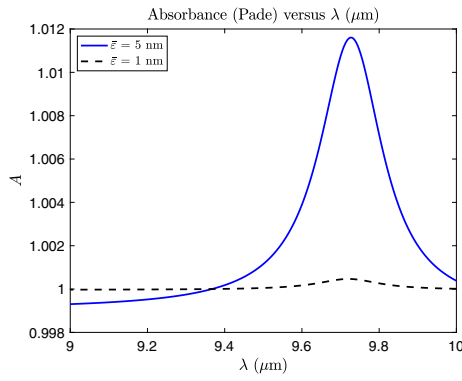


Fig. 5. Slices of the absorbance map for the VGV configuration: plot of the relative absorbance $a(\lambda, \bar{\epsilon}) = A(\lambda, \bar{\epsilon})/A(\lambda, 0)$ versus λ (illumination wavelength), where $\bar{\epsilon} = 1, 5$ nm are particular choices of the amplitude of the graphene sheet deformation. Graphene parameter choices are $E_F = 0.45$ eV and $\Gamma = 2.6 \times 10^{-3}$ eV.

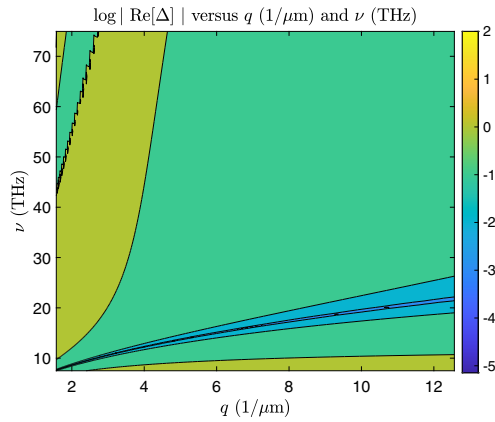


Fig. 6. Plot of the level sets of the natural logarithm of the absolute value of the real part of the dispersion relation, Δ from Eq. (A1), for the VGIg configuration, $\epsilon^{(w)} = 3$. Graphene parameter choices are $E_F = 0.45$ eV and $\Gamma = 2.6 \times 10^{-3}$ eV. Contour plots versus q (wavenumber of surface wave) and ν (illumination frequency).

the introduction of a periodic corrugation of amplitude $\epsilon_{\max} = 5$ nm. We further studied the limits of exciting a GSPR by examining the slice of this absorbance map at $\epsilon = 1$ nm (Fig. 5). In this, we observed a 0.05% enhancement.

B. Vacuum–Graphene–Ion Gel Configuration

We next proceeded to the vacuum–graphene–ion gel (VGIg) set up and examined the dispersion relation, Eq. (A1). In particular, in Figs. 6 and 7, we display $\log \text{Re}\{\Delta\}$ versus (q, ν) and (d, λ) , respectively. As before, these plots indicate the approximate locations of GSPRs in either (q, ν) or (d, λ) space, which informed our choices of simulation parameters. With these, we generated the complete plot of the absorbance map for all values $0 \leq \epsilon \leq \epsilon_{\max}$ in Fig. 8, and for the final slice at $\epsilon = \epsilon_{\max}$ in Fig. 9.

Here we saw a large 50% enhancement in the absorbance (versus the flat-interface configuration) with the introduction of a periodic corrugation of amplitude merely $\epsilon_{\max} = 5$ nm. We further studied the limits of exciting a GSPR by examining

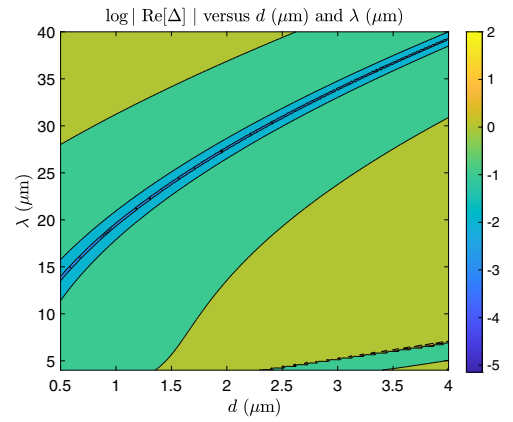


Fig. 7. Plot of the level sets of the natural logarithm of the absolute value of the real part of the dispersion relation, Δ from Eq. (A1), for the VGIg configuration, $\epsilon^{(w)} = 3$. Graphene parameter choices are $E_F = 0.45$ eV and $\Gamma = 2.6 \times 10^{-3}$ eV. Contour plots versus d (period of surface wave) and λ (illumination wavelength).

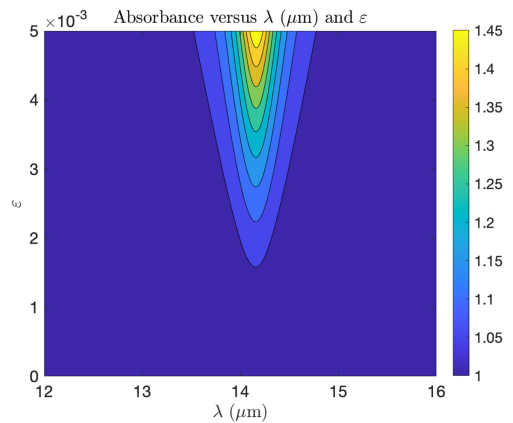


Fig. 8. Complete plot of the absorbance map for the VGIg configuration: contour plot of the relative absorbance $a(\lambda, \epsilon) = A(\lambda, \epsilon)/A(\lambda, 0)$ versus λ (illumination wavelength) and ϵ (amplitude of the graphene sheet deformation). Graphene parameter choices are $E_F = 0.45$ eV and $\Gamma = 2.6 \times 10^{-3}$ eV.

the slice of this absorbance map at $\epsilon = 1$ nm (Fig. 9). In this, we observed a remarkable 2% enhancement.

C. Vacuum–Graphene–Silica Configuration

We concluded with the vacuum–graphene–silica (VGS) configuration and studied the dispersion relation, Eq. (A1). In fact, in Figs. 10 and 11, we display $\log \text{Re}\{\Delta\}$ versus (q, ν) and (d, λ) , respectively. Once again, these plots indicate the approximate locations of GSPRs in either (q, ν) or (d, λ) space, which decided our choices of simulation parameters. With these, we generated the complete plot of the absorbance map for all values $0 \leq \epsilon \leq \epsilon_{\max}$ in Fig. 12, and for the final slice at $\epsilon = \epsilon_{\max}$ in Fig. 13. Here we saw an enormous 60% enhancement in the absorbance (versus the flat-interface configuration) with the introduction of a periodic corrugation of amplitude only $\epsilon_{\max} = 5$ nm. We further studied the limits of exciting a GSPR by examining the slice of this absorbance map

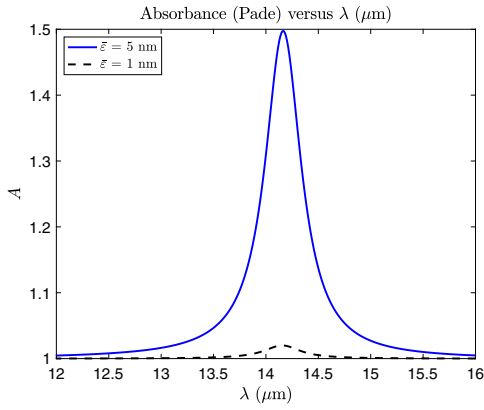


Fig. 9. Slices of the absorbance map for the VGIg configuration: plot of the relative absorbance $a(\lambda, \bar{\varepsilon}) = A(\lambda, \bar{\varepsilon})/A(\lambda, 0)$ versus λ (illumination wavelength), where $\bar{\varepsilon} = 1, 5$ nm are particular choices of the amplitude of the graphene sheet deformation. Graphene parameter choices are $E_F = 0.45$ eV and $\Gamma = 2.6 \times 10^{-3}$ eV.

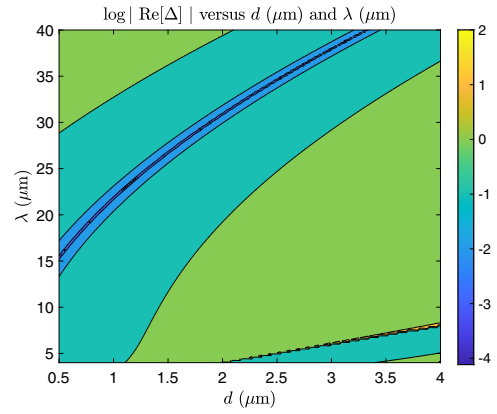


Fig. 11. Plot of the level sets of the natural logarithm of the absolute value of the real part of the dispersion relation, Δ from Eq. (A1), for the VGS configuration, $\epsilon^{(w)} = 4$. Graphene parameter choices are $E_F = 0.45$ eV and $\Gamma = 2.6 \times 10^{-3}$ eV. Contour plots versus d (period of surface wave) and λ (illumination wavelength).

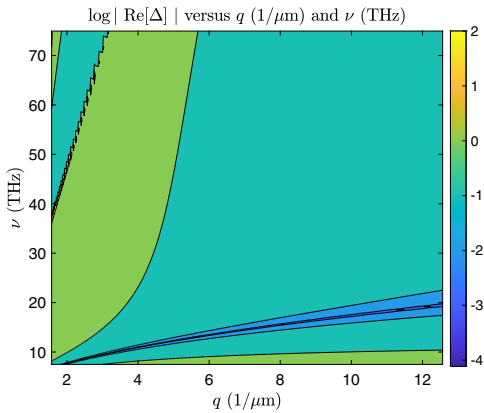


Fig. 10. Plot of the level sets of the natural logarithm of the absolute value of the real part of the dispersion relation, Δ from Eq. (A1), for the VGS configuration, $\epsilon^{(w)} = 4$. Graphene parameter choices are $E_F = 0.45$ eV and $\Gamma = 2.6 \times 10^{-3}$ eV. Contour plots versus q (wavenumber of surface wave) and ν (illumination frequency).

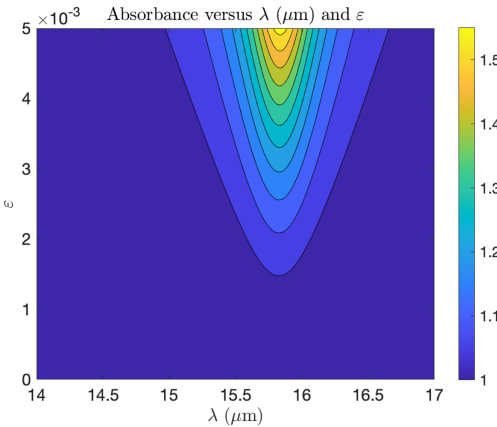


Fig. 12. Complete plot of the absorbance map for the VGS configuration: contour plot of the relative absorbance $a(\lambda, \varepsilon) = A(\lambda, \varepsilon)/A(\lambda, 0)$ versus λ (illumination wavelength) and ε (amplitude of the graphene sheet deformation). Graphene parameter choices are $E_F = 0.45$ eV and $\Gamma = 2.6 \times 10^{-3}$ eV.

at $\varepsilon = 1$ nm (Fig. 13). In this, we observe an impressive 2.3% enhancement.

To close, in Fig. 14, we display a plot of the scaled modulus of the scattered field at $\lambda = 15.8$ μm :

$$\frac{|U(x, z; \bar{\varepsilon})|}{|U(x, z; 0)|}$$

Here we see the significant enhancement of the field at the graphene sheet. In addition, in Fig. 15, we show the scaled reflectance map:

$$b(\lambda, \varepsilon) := \frac{B(\lambda, \varepsilon)}{B(\lambda, 0)},$$

which indicates how much energy is reflected back into the upper layer. It also gives an indication of the magnitude of the scattered field displayed in Fig. 14.

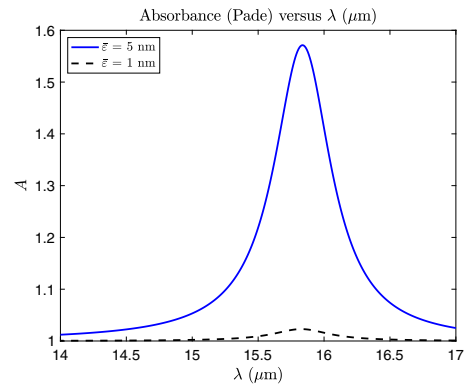


Fig. 13. Slices of the absorbance map for the VGS configuration: plot of the relative absorbance $a(\lambda, \bar{\varepsilon}) = A(\lambda, \bar{\varepsilon})/A(\lambda, 0)$ versus λ (illumination wavelength), where $\bar{\varepsilon} = 1, 5$ nm are particular choices of the amplitude of the graphene sheet deformation. Graphene parameter choices are $E_F = 0.45$ eV and $\Gamma = 2.6 \times 10^{-3}$ eV.

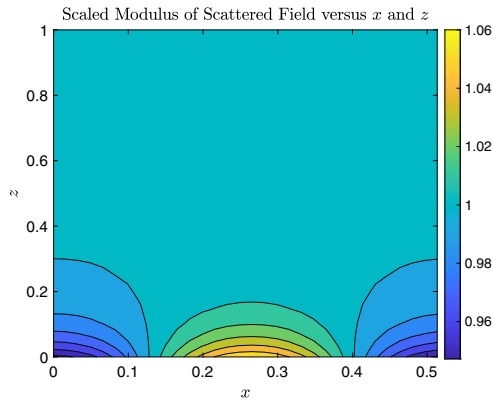


Fig. 14. Plot of the scaled modulus of the scattered field for the VGS configuration at $\lambda = 15.8 \mu\text{m}$ near the GSPR. Graphene parameter choices are $E_F = 0.45 \text{ eV}$ and $\Gamma = 2.6 \times 10^{-3} \text{ eV}$.

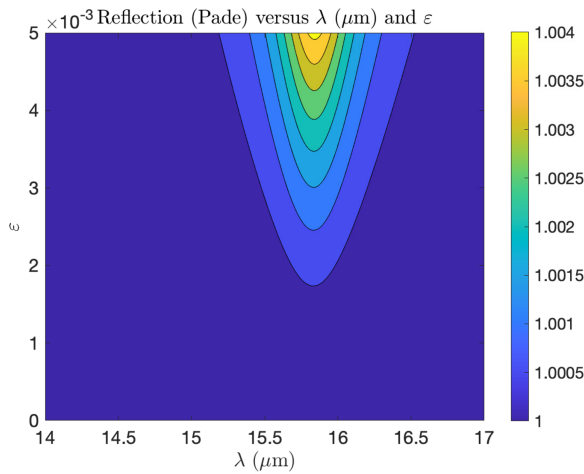


Fig. 15. Complete plot of the reflectance map for the VGS configuration: contour plot of the relative reflection $b(\lambda, \varepsilon) = B(\lambda, \varepsilon)/B(\lambda, 0)$ versus λ (illumination wavelength) and ε (amplitude of the graphene sheet deformation). Graphene parameter choices are $E_F = 0.45 \text{ eV}$ and $\Gamma = 2.6 \times 10^{-3} \text{ eV}$.

5. CONCLUSION

In this paper, we have revisited our previous numerical experiments on metal plasmons launched by vanishingly small grating structures [15] in the presence of graphene. These simulations were generated by our rapid and robust HOS scheme [16], and with it we conclusively demonstrated how the plasmonic response of a perfectly flat sheet of graphene can be significantly altered with even a tiny corrugation. With this, we have concluded that it is of extraordinary importance to utilize fabrication techniques producing interfaces whose deviations from flat are on the order of angstroms [32,33].

Beyond the simple device geometries used in this work, our method can be used for a wide range of van der Waals heterostructures [34] as well as graphene-on-a-mirror configurations, which can support acoustic graphene plasmons [5,6,35–37] or image polaritons in other two-dimensional materials [38,39].

APPENDIX A: DISPERSION RELATION FOR GRAPHENE SURFACE PLASMONS

In this appendix, we derive the dispersion relation for graphene surface plasmons in our modern formulation. For this, it is helpful to have the flat-interface ($g \equiv 0$) DNOs at hand [16]:

$$G(0)U = \sum_{p=-\infty}^{\infty} (-i\gamma_p^{(u)}) \hat{U}_p e^{i\alpha_p x},$$

$$J(0)W = \sum_{p=-\infty}^{\infty} (-i\gamma_p^{(w)}) \hat{W}_p e^{i\alpha_p x},$$

where, for $m \in \{u, w\}$,

$$\alpha_p := \alpha + \left(\frac{2\pi}{d}\right)p, \quad \gamma_p^{(m)} := \sqrt{\epsilon^{(m)}k_0^2 - \alpha_p^2}, \quad \text{Im}\{\gamma_p^{(m)}\} \geq 0.$$

Following the literature [31], we seek solutions to Eq. (1) of the form

$$u(x, z) = e^{iqx - \kappa^{(u)}z}, \quad z > g(x),$$

$$w(x, z) = e^{iqx + \kappa^{(w)}z}, \quad z < g(x).$$

To solve the Helmholtz equations, Eqs. (1a) and (1b), we require

$$\kappa^{(m)} = \sqrt{q^2 - \epsilon^{(m)}k_0^2}, \quad m \in \{u, w\},$$

so that we can identify $q = \alpha_1$ and $\kappa^{(m)} = i\gamma_1^{(m)}$. To capture the behavior we seek, we require that

$$q \in \mathbf{R}, \quad \kappa^{(u)} \in \mathbf{R}^+, \quad \kappa^{(w)} \in \mathbf{R}^+,$$

so that solutions are laterally periodic, and decay away from the interface. We note that

$$v = \frac{c_0}{\lambda}, \quad \omega = 2\pi v = \frac{2\pi c_0}{\lambda} = c_0 k_0,$$

$$E = \hbar\omega = \frac{2\pi \hbar c_0}{\lambda}, \quad k_0 = \frac{\omega}{c_0} = \frac{2\pi}{\lambda}, \quad d = \frac{2\pi}{q}.$$

To satisfy the boundary conditions, Eqs. (1c) and (1d), these solutions must satisfy the *dispersion relation*

$$\Delta(d, \lambda) = \Delta(q, \omega) = \frac{\epsilon^{(u)}}{\kappa^{(u)}} + \frac{\epsilon^{(w)}}{\kappa^{(w)}} + \frac{i\hat{\sigma}^{(g)}}{k_0} = 0. \quad (\text{A1})$$

We note that for $\kappa^{(m)}$ to be real, we require

$$q^2 > \epsilon^{(m)}k_0^2 \Rightarrow \frac{2\pi}{d} > \sqrt{\epsilon^{(m)}}\frac{2\pi}{\lambda} \Rightarrow d < \frac{\lambda}{\sqrt{\epsilon^{(m)}}}.$$

We rewrite the dispersion relation, Eq. (A1), as

$$\frac{\epsilon^{(u)}}{\kappa^{(u)}} + \frac{\epsilon^{(w)}}{\kappa^{(w)}} = \frac{\text{Im}\{\hat{\sigma}^{(g)}\}}{k_0} - i\frac{\text{Re}\{\hat{\sigma}^{(g)}\}}{k_0},$$

so that if $\epsilon^{(u)}, \epsilon^{(w)} \in \mathbf{R}^+$, it is necessary that

$$\text{Im}\{\hat{\sigma}^{(g)}\} > 0.$$

Funding. National Science Foundation (DMS-1813033, ECCS-1809723).

Acknowledgment. D.P.N. gratefully acknowledges support from the National Science Foundation. S.H.O. gratefully acknowledges support from the National Science Foundation and the Sanford P. Bordeau Endowed Chair in Electrical Engineering at the University of Minnesota. The authors thank In-Ho Lee for valuable thoughts and insights on this work.

Disclosures. The authors declare no conflicts of interest.

Data Availability. Data underlying the results presented in this paper are not publicly available at this time but may be obtained from the authors upon reasonable request.

REFERENCES

1. F. Bonaccorso, Z. Sun, T. Hasan, and A. C. Ferrari, "Graphene photonics and optoelectronics," *Nat. Photonics* **4**, 611–622 (2010).
2. A. N. Grigorenko, M. Polini, and K. S. Novoselov, "Graphene plasmonics," *Nat. Photonics* **6**, 749–758 (2012).
3. T. Low, A. Chaves, J. Caldwell, A. Kumar, N. Fang, P. Avouris, T. Heinz, F. Guinea, L. Martin-Moreno, and F. Koppens, "Polaritons in layered two-dimensional materials," *Nat. Mater.* **16**, 182–194 (2017).
4. D. N. Basov, M. M. Fogler, and F. J. Garcia de Abajo, "Polaritons in van der Waals materials," *Science* **354**, aag1992 (2016).
5. D. A. Iranzo, S. Nanot, E. J. C. Dias, I. Epstein, C. Peng, D. K. Efetov, M. B. Lundberg, R. Parret, J. Osmond, J.-Y. Hong, J. Kong, D. R. Englund, N. M. R. Peres, and F. H. L. Koppens, "Probing the ultimate plasmon confinement limits with a van der Waals heterostructure," *Science* **360**, 291–295 (2018).
6. I.-H. Lee, D. Yoo, P. Avouris, T. Low, and S.-H. Oh, "Graphene acoustic plasmon resonator for ultrasensitive infrared spectroscopy," *Nat. Nanotechnol.* **14**, 313–319 (2019).
7. M. Jablan, H. Buljan, and M. Soljačić, "Plasmonics in graphene at infrared frequencies," *Phys. Rev. B* **80**, 245435 (2009).
8. F. H. L. Koppens, D. E. Chang, and F. J. Garcia de Abajo, "Graphene plasmonics: a platform for strong light-matter interactions," *Nano Lett.* **11**, 3370–3377 (2011).
9. M. Jablan, M. Soljačić, and H. Buljan, "Plasmons in graphene: fundamental properties and potential applications," *Proc. IEEE* **101**, 1689–1704 (2013).
10. A. Audatore, C. de Angelis, A. Locatelli, and A. B. Aceves, "Tuning of surface plasmon polaritons beat length in graphene directional couplers," *Opt. Lett.* **38**, 4228–4231 (2013).
11. F. J. G. de Abajo, "Graphene plasmonics: challenges and opportunities," *ACS Photon.* **1**, 135–152 (2014).
12. T. Low and P. Avouris, "Graphene plasmonics for terahertz to mid-infrared applications," *ACS Nano* **8**, 1086 (2014).
13. J. Chen, M. Badioli, P. Alonso-Gonzalez, S. Thongrattanasiri, F. Huth, J. Osmond, M. Spasenovic, A. Centeno, A. Pesquera, P. Godignon, A. Zurutuza Elorza, N. Camara, F. J. G. de Abajo, R. Hillenbrand, and F. H. L. Koppens, "Optical nano-imaging of gate-tunable graphene plasmons," *Nature* **487**, 77–81 (2012).
14. Z. Fei, A. S. Rodin, G. O. Andreev, W. Bao, A. S. McLeod, M. Wagner, L. M. Zhang, Z. Zhao, M. Thiemens, G. Dominguez, M. M. Fogler, A. H. C. Neto, C. N. Lau, F. Keilmann, and D. N. Basov, "Gate-tuning of graphene plasmons revealed by infrared nano-imaging," *Nature* **487**, 82–85 (2012).
15. D. P. Nicholls, S.-H. Oh, T. W. Johnson, and F. Reitich, "Launching surface plasmon waves via vanishingly small periodic gratings," *J. Opt. Soc. Am. A* **33**, 276–285 (2016).
16. D. P. Nicholls, "Numerical simulation of grating structures incorporating two-dimensional materials: a high-order perturbation of surfaces framework," *SIAM J. Appl. Math.* **78**, 19–44 (2018).
17. M. Maier, D. Margetis, and M. Lusk, "Dipole excitation of surface plasmon on a conducting sheet: finite element approximation and validation," *J. Comput. Phys.* **339**, 126–145 (2017).
18. J. H. Song, M. Maier, and M. Lusk, "Adaptive finite element simulations of waveguide configurations involving parallel 2D material sheets," *Comput. Methods Appl. Mech. Eng.* **351**, 20–34 (2019).
19. M. Maier, D. Margetis, and M. Lusk, "Generation of surface plasmon-polaritons by edge effects," *Commun. Math. Sci.* **16**, 77–95 (2018).
20. M. Maier, M. Mattheakis, E. Kaxiras, M. Lusk, and D. Margetis, "Homogenization of plasmonic crystals: seeking the epsilon-near-zero effect," *Proc. R. Soc. A* **475**, 20190220 (2019).
21. B. Gallinet, J. Butet, and O. J. F. Martin, "Numerical methods for nanophotonics: standard problems and future challenges," *Laser Photon. Rev.* **9**, 577–603 (2015).
22. R. Petit, ed., *Electromagnetic Theory of Gratings* (Springer, 1980).
23. P. Yeh, *Optical Waves in Layered Media* (Wiley-Interscience, 2005).
24. Y. Bludov, A. Ferreira, N. Peres, and M. Vasilevskiy, "A primer on surface plasmon-polaritons in graphene," *Int. J. Mod. Phys. B* **27**, 1341001 (2013).
25. D. P. Nicholls, "On analyticity of linear waves scattered by a layered medium," *J. Differ. Equ.* **263**, 5042–5089 (2017).
26. D. P. Nicholls and F. Reitich, "Analytic continuation of Dirichlet-Neumann operators," *Numer. Math.* **94**, 107–146 (2003).
27. D. Gottlieb and S. A. Orszag, *Numerical Analysis of Spectral Methods: Theory and Applications*, Vol. 26 of CBMS-NSF Regional Conference Series in Applied Mathematics (Society for Industrial and Applied Mathematics, 1977).
28. J. Shen, T. Tang, and L.-L. Wang, *Spectral Methods-Algorithms, Analysis and Applications*, Vol. 41 of Springer Series in Computational Mathematics (Springer, 2011).
29. G. A. Baker, Jr. and P. Graves-Morris, *Padé Approximants*, 2nd ed. (Cambridge University, 1996).
30. C. M. Bender and S. A. Orszag, *Advanced Mathematical Methods for Scientists and Engineers*, International Series in Pure and Applied Mathematics (McGraw-Hill Book, 1978).
31. P. A. D. Goncalves and N. M. R. Peres, *An Introduction to Graphene Plasmonics* (World Scientific, 2016).
32. P. Nagpal, N. C. Lindquist, S.-H. Oh, and D. J. Norris, "Ultrasmooth patterned metals for plasmonics and metamaterials," *Science* **325**, 594–597 (2009).
33. N. C. Lindquist, P. Nagpal, K. M. McPeak, D. J. Norris, and S.-H. Oh, "Engineering metallic nanostructures for plasmonics and nanophotonics," *Rep. Prog. Phys.* **75**, 036501 (2012).
34. A. K. Geim and I. V. Grigorieva, "Van der Waals heterostructures," *Nature* **499**, 419–425 (2013).
35. E. Hwang and S. D. Sarma, "Plasmon modes of spatially separated double-layer graphene," *Phys. Rev. B* **80**, 205405 (2009).
36. P. Alonso-Gonzalez, A. Y. Nikitin, Y. Gao, A. Woessner, M. B. Lundberg, A. Principi, N. Forcellini, W. Yan, S. Velez, A. J. Huber, K. Watanabe, T. Taniguchi, F. Casanova, L. E. Hueso, M. Polini, J. Hone, F. H. L. Koppens, and R. Hillenbrand, "Acoustic terahertz graphene plasmons revealed by photocurrent nanoscopy," *Nat. Nanotechnol.* **12**, 31–35 (2017).
37. I. Epstein, D. Alcaraz, Z. Huang, V.-V. Pusapati, J.-P. Hugonin, A. Kumar, X. M. Deputy, T. Khodkov, T. G. Rappoport, J.-Y. Hong, N. M. R. Peres, J. Kong, D. R. Smith, and F. H. L. Koppens, "Far-field excitation of single graphene plasmon cavities with ultracompressed mode volumes," *Science* **368**, 1219–1223 (2020).
38. I.-H. Lee, M. He, X. Zhang, Y. Luo, S. Liu, J. H. Edgar, K. Wang, P. Avouris, T. Low, J. D. Caldwell, and S.-H. Oh, "Image polaritons in boron nitride for extreme polariton confinement with low losses," *Nat Commun* **11**, 3649 (2020).
39. D. N. Basov, A. Asenjo-Garcia, P. J. Schuck, X. Zhu, and A. Rubio, "Polariton panorama," *Nanophotonics* **10**, 549–577 (2021).